Science Advances
AAAS

Supplementary Materials for

Noninvasive measurements of spin transport properties of an antiferromagnetic insulator

Hailong Wang, Shu Zhang, Nathan J. McLaughlin, Benedetta Flebus, Mengqi Huang,
Yuxuan Xiao, Chuanpu Liu, Mingzhong Wu, Eric E. Fullerton,
Yaroslav Tserkovnyak, Chunhui Rita Du*

*Corresponding author. Email: c1du@physics.ucsd.edu

This PDF file includes:

Supplementary Text

Section S1. Extraction of Nitrogen Vacancy Spin Relaxation Rates

An NV center has an $S = 1$ electron spin and serves as a three-level quantum impurity. Figure S3A shows the energy levels of an NV spin as a function of an external magnetic field H applied along the NV-axis. For $H = 0$, the $m_s = \pm 1$ states are degenerate and the corresponding electron spin resonance (ESR) frequency equals 2.87 GHz. For $H > 0$, the Zeeman coupling separates the $m_s = -1$ and the $m_s = +1$ spin states by an energy gap equaling $2\tilde{\gamma}H$, where $\tilde{\gamma}$ denotes the gyromagnetic ratio of the NV spin. This three-level spin system can be optically accessed by spin-dependent photoluminescence (PL), where the $m_s = \pm 1$ spin states are more likely to be trapped by a non-radiative pathway (in the red wavelength range) through an intersystem crossing and back to the $m_s = 0$ ground state, yielding a significantly reduced PL intensity.

Fluctuating magnetic fields at the NV ESR frequencies can induce $m_s = 0 \leftrightarrow \pm 1$ transitions as illustrated in Fig. S3B, which can be optically accessed by NV relaxometry measurements via spin-dependent PL. NV measurements were performed in a custom designed Montana s200 closed-loop optical cryostat (Montana instruments) operational from 4 K to 350 K. Figures S3C and S3D show two sets of spin relaxation data measured on an NV center (NV$_1$) positioned on the surface of an α-Fe$_2$O$_3$ crystal. The external magnetic field H is set to be $H = 720$ Oe and 405 Oe, respectively. To extract the NV relaxation rates $\Gamma_\pm$, we fit the time-dependent PL data into following equation, which is based on a three-level model (*34, 43*):

$$\frac{d}{dt}\begin{pmatrix} P_0(t) \\ P_+(t) \\ P_-(t) \end{pmatrix} = \begin{pmatrix} -(\Gamma_+ + \Gamma_-) & \Gamma_+ & \Gamma_- \\ \Gamma_+ & -\Gamma_+ & 0 \\ \Gamma_- & 0 & -\Gamma_- \end{pmatrix} \begin{pmatrix} P_0(t) \\ P_+(t) \\ P_-(t) \end{pmatrix} \tag{S1}$$

Here, P_0, P_+, and P_- are the probabilities of an NV spin at the $m_s = 0$, $m_s = +1$, and $m_s = -1$ states, respectively, Γ_+ and Γ_- characterize the spin relaxation rates of the $m_s = 0 \leftrightarrow +1$ and $m_s = 0 \leftrightarrow -1$ transitions. Note that the magnetic noise generated by the α-Fe$_2$O$_3$ crystal will not affect the $m_s = +1 \leftrightarrow -1$ transition at the leading order of the dipolar coupling, therefore, the corresponding relaxation rate is set to zero. By fitting the results shown in Figs. S3C and S3D to Eq. (S1), we are able to extract the NV relaxation rate $\Gamma_\pm$. When positioned on an insulating nonmagnetic substrate, the measured NV relaxation rate becomes comparable to the intrinsic value, which is at least one order of magnitude smaller than the value measured on an α-Fe$_2$O$_3$ crystal as shown in Fig. S4, suggesting non-magnetic sources of NV relaxation do not play a major role in our experiments.

Section S2. Inferring the Intrinsic Spin Diffusion Constant of a Proximal Magnetic Insulator from the NV Relaxation Rates

In this section, we provide detailed calculations to relate the measured NV relaxation rate induced by the longitudinal spin noise to the intrinsic spin diffusion constant of a proximal magnetic insulator. Figure S5 shows the coordinate system used for our analysis. We assume that the magnetic insulator occupies the space Ω with $z \leq 0$, and its surface lies in the x-y plane. In the global frame, the time-dependent stray field $\mathbf{B}_s$ generated by a fluctuating spin distribution $\mathbf{s}$ in the magnetic insulator is

$$\mathbf{B}_s(\mathbf{r},t) = \gamma \int_\Omega d^3\mathbf{r}' \mathcal{D}(\mathbf{r},\mathbf{r}') \mathbf{s}(\mathbf{r}',t), \tag{S2}$$

where $\mathcal{D}(\mathbf{r},\mathbf{r}') = -\nabla_\mathbf{r}\nabla_{\mathbf{r}'}(1/|\mathbf{r}-\mathbf{r}'|)$ is the magnetostatic Green's function tensor and γ is the gyromagnetic constant of the magnetic insulator. Assuming that the orientation of the NV center $\mathbf{n}$ lies in the y-z plane, and Eq. (S4) is the rotational matrix such that $\mathcal{R}_x(\theta)\mathbf{n} = \mathbf{z}$, the stray field at the position of the NV center $\mathbf{r}_0 = (0,0,d)$ can be projected into the local frame of the NV:

$$\mathbf{B} = \mathcal{R}_x(\theta)\mathbf{B}_s(\mathbf{r}_0,t), \tag{S3}$$

where

$$\mathcal{R}_x(\theta) = \begin{pmatrix} 1 & 0 & 0 \\ 0 & \cos\theta & -\sin\theta \\ 0 & \sin\theta & \cos\theta \end{pmatrix}. \tag{S4}$$

NV quantum spin $\mathbf{S}$ interacts with the stray field through Zeeman coupling:

$$\mathcal{H}_{\text{int}} = -\tilde{\gamma}\mathbf{B}\cdot\mathbf{S} = -\frac{\tilde{\gamma}}{2}\left(S^-B^+ + S^+B^- + 2S^zB^z\right), \tag{S5}$$

where $B^\pm = B^x \pm iB^y$ and $S^\pm = S^x \pm iS^y$ are in terms of the components in the NV local frame, and $\tilde{\gamma}$ is the gyromagnetic constant of the NV spin. The NV relaxation rate (38) at its ESR frequency ω can be obtained by the time-dependent perturbation theory:

$$\Gamma(\omega) = \frac{\tilde{\gamma}^2}{2}\int dt\, e^{i\omega t}\left\langle\left\{B^+(t), B^-(0)\right\}\right\rangle, \tag{S6}$$

where the Fourier transform is taken for the symmetrical temporal correlation functions of the local magnetic field at the NV site. We remark that only the stray field fluctuations transverse to the NV axis affect the NV transition rate.

We now look at the demagnetization kernel (49) with the help of the following identity:

$$\frac{1}{|\mathbf{r}-\mathbf{r}'|} = \int \frac{d^2\mathbf{k}}{(2\pi)^2}\frac{2\pi}{k_\perp}e^{-k_\perp|z-z'|}e^{i\mathbf{k}_\perp\cdot(\mathbf{r}_\perp-\mathbf{r}_\perp')}, \tag{S7}$$

where $\mathbf{k}_\perp = (k_x,k_y,0)$, $\mathbf{r}_\perp = (x,y,0)$ and we obtain for $\alpha,\beta = x,y$

$$\begin{cases} D_{\alpha\beta}(\mathbf{k},d) = -2\pi\left(k_\alpha k_\beta/k_\perp\right)e^{-k_\perp(d-z)}, \\ D_{\alpha z}(\mathbf{k},d) = -2\pi i k_\alpha e^{-k_\perp(d-z)}, \\ D_{zz}(\mathbf{k},d) = 2\pi k_\perp e^{-k_\perp(d-z)}. \end{cases} \tag{S8}$$

Combining with Eq.(S2) and Eq. (S3),

$$B^-(t) = \gamma\int_\Omega d^3\mathbf{r}\left[C_{\theta,d,\mathbf{r}}^x s^x(\mathbf{r},t) + C_{\theta,d,\mathbf{r}}^y s^y(\mathbf{r},t) + C_{\theta,d,\mathbf{r}}^z s^z(\mathbf{r},t)\right], \tag{S9}$$

where

$$
\begin{cases}
C_{\theta,d,\mathbf{r}}^{x} = D_{xx} - iD_{yx}\cos\theta + iD_{zx}\sin\theta, \\
C_{\theta,d,\mathbf{r}}^{y} = D_{xy} - iD_{yy}\cos\theta + iD_{zy}\sin\theta, \\
C_{\theta,d,\mathbf{r}}^{z} = D_{xz} - iD_{yz}\cos\theta + iD_{zz}\sin\theta.
\end{cases}
\tag{S10}
$$

In the following, we focus only on the spin fluctuation $s_\parallel$ along the order parameter, which is relevant for the rate measurement performed at NV ESR frequencies lower than the magnon gap. For an order parameter of the magnetic insulator pointing in an arbitrary direction with global spherical angles (ϑ,φ), $\mathbf{s} = (s^x, s^y, s^z) = (\sin\vartheta\cos\varphi, \sin\vartheta\sin\varphi, \cos\vartheta)s_\parallel$. Therefore, the NV relaxation rate

$$
\Gamma_L(\omega) = \frac{(\gamma\tilde{\gamma})^2}{2}\int_{-\infty}^{0} dz \int_{-\infty}^{0} dz' \int \frac{d^2\mathbf{k}_\perp}{(2\pi)^2}\left(C_{\theta,d,z,\mathbf{k}_\perp}\right)^* C_{\theta,d,z',\mathbf{k}_\perp} \mathcal{S}(z,z',\mathbf{k}_\perp;\omega),
\tag{S11}
$$

turns out to be determined by the correlation function:

$$
\mathcal{S}(z,z',\mathbf{k}_\perp;\omega) = \int dt \int d^2(\mathbf{r}_\perp - \mathbf{r}'_\perp) e^{i\omega t - i\mathbf{k}_\perp\cdot(\mathbf{r}_\perp - \mathbf{r}'_\perp)}\left\langle\{s_\parallel(\mathbf{r},t), s_\parallel(\mathbf{r}',0)\}\right\rangle,
\tag{S12}
$$

and

$$
C_{\theta,d,z,\mathbf{k}_\perp} = \int d^2\mathbf{r}_\perp e^{-i\mathbf{k}_\perp\cdot\mathbf{r}_\perp}\left(C_{\theta,d,\mathbf{r}}^{x}\sin\vartheta\cos\varphi + C_{\theta,d,\mathbf{r}}^{y}\sin\vartheta\sin\varphi + C_{\theta,d,\mathbf{r}}^{z}\cos\vartheta\right).
\tag{S13}
$$

The fluctuation-dissipation theorem relates the correlation function to the imaginary part of the dynamical longitudinal spin susceptibility χ'':

$$
\mathcal{S}(z,z',\mathbf{k}_\perp;\omega) = \hbar\coth\left(\frac{\beta\hbar\omega}{2}\right)\chi''(z,z',\mathbf{k}_\perp;\omega) \overset{\beta\hbar\omega\ll 1}{\approx} \frac{2}{\beta\omega}\chi''(z,z',\mathbf{k}_\perp;\omega),
\tag{S14}
$$

where $\beta = 1/k_B T$, k_B is the Boltzmann constant, and T is the temperature. For experiments near room temperature, we take the classical limit $\beta\hbar\omega \ll 1$. Inserting Eq. (S14) into Eq. (S11), the NV relaxation rate becomes

$$
\Gamma_L(\omega) = \frac{1}{\beta\omega}f(\theta,\vartheta,\varphi)\int dk_\perp k_\perp^{3} e^{-2k_\perp d}\int dz \int dz' e^{2k_\perp z}\chi'',
\tag{S15}
$$

where the integration over the direction of $\mathbf{k}_\perp$ has been performed to give the geometric factor

$$
f(\theta,\vartheta,\varphi) = \frac{(\gamma\tilde{\gamma})^2\pi}{8}\left[(5 - \cos 2\theta)(3 + \cos 2\vartheta) + 2\sin^2\theta\sin^2\vartheta\cos 2\varphi\right].
\tag{S16}
$$

We have assumed axial symmetry such that χ'' depends only on the length of $\mathbf{k}_\perp$.

To find the dynamical susceptibility χ'', we consider a weakly-interacting magnon system where spin density dynamics can be treated as diffusive at length scales larger than the magnon mean free path (*38*). For a homogeneous system in the absence of magnetic fields,

$$
\partial_t s_\parallel + \nabla\cdot\mathbf{j}_s = -\frac{1}{\tau_s}s_\parallel.
\tag{S17}
$$

Here, we have introduced the spin-relaxation time τ_s and the spin current $\mathbf{j}_s = -\sigma\nabla\mu$, where σ is the spin conductivity, $\mu = s_\parallel/\chi_0$ is the spin chemical potential, and χ_0 is the static uniform

longitudinal susceptibility. Note that the longitudinal spin susceptibility χ_0 is largely governed by exchange interaction when close to the room temperature, being weakly affected by the anisotropy or Dzyaloshinskii-Moriya interaction. Thus, we expect that χ_0 does not exhibit a significant variation across the Morin transition temperature. In the presence of an external magnetic field H, $\mu = s_\| / \chi_0 - H$ and spin density relaxes towards $\chi_0 H$:

$$\partial_t s_\| + \nabla \cdot \mathbf{j}_s = -\frac{1}{\tau_s}\left(s_\| - \chi_0 H\right). \tag{S18}$$

By introducing diffusion coefficient $D = \sigma / \chi_0$, we can get:

$$\left(\partial_t + \frac{1}{\tau_s}\right)\mu - D\nabla^2\mu = -\partial_t H. \tag{S19}$$

Imposing the experimental boundary condition $j_s^{\,z}(z=0)=0$ (no spin current flows out of the sample), the Green function is:

$$G(\mathbf{r},\mathbf{r}';t,t') = \frac{1}{\left[4\pi D(t-t')\right]^{3/2}} e^{-\left[(x-x')^2+(y-y')^2\right]/4D(t-t')}\left(e^{-(z-z')^2/4D(t-t')} + e^{-(z+z')^2/4D(t-t')}\right)e^{-(t-t')/\tau_s}. \tag{S20}$$

Therefore,

$$\mu(\mathbf{r},t) = -\int_\Omega d^3\mathbf{r}'\int_{-\infty}^t dt'\, G(\mathbf{r},\mathbf{r}';t,t')\partial_{t'}H(\mathbf{r}',t')$$

$$= \int_\Omega d^3\mathbf{r}'\int_{-\infty}^t dt'\, G(\mathbf{r},\mathbf{r}';t,t')\int\frac{d^2\mathbf{k}'_\perp}{(2\pi)^2}\int\frac{d\omega'}{2\pi}i\omega' H(z',\mathbf{k}'_\perp,\omega')e^{i\mathbf{k}'_\perp\cdot\mathbf{r}'_\perp - i\omega' t'}. \tag{S21}$$

The Fourier transform of Eq. (S21) yields

$$\mu(z,\mathbf{k}_\perp,\omega) = \int d^2\mathbf{r}_\perp\int dt\, e^{i\omega t - i\mathbf{k}_\perp\cdot\mathbf{r}_\perp}\mu(\mathbf{r},t)$$

$$= i\omega\int_{-\infty}^0 dz'\, G(z,z',\mathbf{k}_\perp;\omega)H(z',\mathbf{k}_\perp,\omega), \tag{S22}$$

where

$$G(z,z',\mathbf{k}_\perp;\omega) = \int d^2\left(\mathbf{r}_\perp - \mathbf{r}_\perp'\right)\int_0^\infty d(t-t')G(z,z',\mathbf{r}_\perp - \mathbf{r}'_\perp;t-t')e^{i\omega(t-t')-i\mathbf{k}_\perp\cdot(\mathbf{r}_\perp - \mathbf{r}'_\perp)}$$

$$= \frac{1}{2Dk_\perp b}\left(e^{-k_\perp b|z-z'|} + e^{-k_\perp b|z+z'|}\right), \tag{S23}$$

with $b = \sqrt{(-i\omega + 1/\tau_s)/Dk_\perp^2 + 1}$ and $\mathrm{Re}[b] > 0$ taken. Invoking $\mu = s_\| / \chi_0 - H$, we obtain the dynamic spin susceptibility:

$$\chi(z,z',\mathbf{k}_\perp;\omega) = \left[i\omega G(z,z',\mathbf{k}_\perp;\omega) + \delta(z-z')\right]\chi_0. \tag{S24}$$

Inserting this into Eq. (S15) results in the relaxation rate:

$$\Gamma_L(\omega) = \frac{\chi_0}{2\beta D} f(\theta,\vartheta,\varphi) \int dk_\perp k_\perp^3 e^{-2k_\perp d} \int_{-\infty}^0 dz \int_{-\infty}^0 dz' e^{2k_\perp z} \mathrm{Im}\left[\frac{i}{k_\perp b}\left(e^{-k_\perp b|z-z'|} + e^{-k_\perp b|z+z'|} \right) \right]$$
$$= \frac{\chi_0}{2\beta D} f(\theta,\vartheta,\varphi) \int_0^\infty dk_\perp e^{-2k_\perp d} \mathrm{Re}\left[\frac{2+b}{b(b+1)^2} \right], \tag{S25}$$

where b carries ω dependence. Since the magnetostatic kernel contributes a factor of $k_\perp^2 e^{-2kd}$ which peaks at $k_\perp \sim 1/d$, in the wavevector integral, the NV relaxation rate is mostly determined by the dynamic susceptibility χ'' at $k_\perp \sim 1/d$, and thus $b \sim \sqrt{-i\omega/Dk_\perp^2 + (d/l_s)^2 + 1}$, where $l_s = \sqrt{D\tau_s}$ is the spin diffusion length. In the limit of a slow relaxation $\tau_s \to \infty$, where the spin diffusion length is much larger than the NV-to-sample distance: $l_s \gg d$, Eq. (S25) can be approximated as:

$$\Gamma_L(\omega) = \frac{\chi_0}{\beta\omega} f(\theta,\vartheta,\varphi) \int_0^\infty dk_\perp k_\perp^2 e^{-2k_\perp d} \frac{\sin\phi + \sin(\phi/2)/\sqrt{\sec\phi}}{1 + \sec\phi + 2\cos(\phi/2)\sqrt{\sec\phi}}, \tag{S26}$$

where $\phi = \tan^{-1}\left(\omega/Dk_\perp^2 \right)$. In the limit of a fast relaxation, $\tau_s \to 0$, where $l_s \ll d$, $\frac{2+b}{b(b+1)^2} \to k_\perp^2 D\tau_s$, and we have

$$\Gamma_L(\omega) \to \frac{\chi_0}{8\beta\omega} f(\theta,\vartheta,\varphi) \frac{\omega\tau_s}{d^3}. \tag{S27}$$

In our experiments, the spin diffusion length is much larger than the NV-to-sample distance $l_s \gg d$, we thus use Eq. (S26) to fit the NV relaxometry results. Figures S6A to S6H show the external magnetic field H and ESR frequency dependence of the NV relaxation rates $\Gamma_\pm$ measured in the prepared NV-α-Fe$_2$O$_3$ device at 229, 260, 265, and 295 K. The variation of the NV relaxation rate agrees well with the theoretical model, which confirms our diffusive treatment of the spin dynamics. From the fitting, we extract the intrinsic spin diffusion constant at individual temperatures.

We further remark that while a theoretical evaluation of the spin diffusion constant D from microscopic material parameters can be complicated by Dzyaloshinskii-Moriya interaction and magnetic anisotropy etc., experimental extraction of D via the NV relaxometry method only requires knowledge on relevant information of NV sensors including: NV-to-sample distance, relative NV orientation, NV ESR frequency, and measured NV relaxation rates. Our work offers a strategy to experimentally measure the spin diffusion constant of a magnetic system without a detailed knowledge of its fundamental material parameters. The presented method is generally applicable to the conventional colinearly ordered (ferro-, antiferro-, or ferri-) magnets, where exchange dominates and frustration is low, we expect the spin transport and thermodynamic properties to be dominated by thermal magnons, whenever the temperature is less but still of the same order as the ordering temperature. Extended NV relaxometry measurement results of a ferrimagnetic insulator Y$_3$Fe$_5$O$_{12}$ sample is presented in Section 6. It would be interesting to study exotic spin transport that deviates from the diffusive picture discussed here in future NV experiments, for example on strong-frustrated magnetic systems or at very low temperatures.

Section S3. Characterization of Distances Between NV Centers and Sample Surface

Nanoscale proximity of NV centers to the α-Fe$_2$O$_3$ crystal is crucial to establishing a strong dipolar coupling between NV centers and the local spin fluctuations. Here, we characterized the NV-to-diamond-surface distance for the two NV centers (NV$_1$ and NV$_2$) used in our measurements. We positioned the diamond nanobeams on top of a 100-nm-thick Y$_3$Fe$_5$O$_{12}$ (YIG) film (*35*). In the low magnetic field regime, the NV ESR frequencies are above the minimal magnon energy and the transverse spin fluctuations dominate the NV spin transitions. Figures S7A and S7B show the measured NV relaxation rates Γ_- of NV$_1$ and NV$_2$ as a function of the external magnetic field H. The measured NV relaxation rates depend on many material parameters including the NV-to-sample distance d and can be theoretically modeled as follows (*34*):

$$\Gamma_- = C \frac{k_B T}{\hbar \omega_-^2} \int \left(\sin^4(\phi_k) + \cos^2(\theta) \frac{\sin^2(2\phi_k)}{4} + \sin^2(\theta) \sin^2(\phi_k) \right) \frac{W k e^{-2dk}(1-e^{-2t_{YIG}k})}{W^2 + [\omega(k,\phi_k)-\omega_-]^2} k \, dk \, d\phi_k \qquad (S28)$$

where C is a constant, T is the temperature, ω_- is the NV ESR frequency for the $m_s = 0 \leftrightarrow -1$ transition, k_B is the Boltzmann constant, θ characterizes the angle of the NV-axis with respect to the normal of the sample surface, d is the NV-to-sample distance, t_{YIG} is the thickness of the YIG film. Please note the frequency dependence of $1/\omega_-^2$ in the prefactor is in contrast to $1/\omega_-$ in Eq. (S5) in Ref. 34. The extra power of inverse frequency is needed to properly account for the strong ellipticity of magnetic precession at low fields (*50*). The Lorentzian factor in the integrand stems from the magnetic response, while the trigonometric factor reflects the magnetostatic response kernel. $f(k,\phi_k)$ is the magnon dispersion function, ϕ_k characterizes the angle between wavevector and in-plane projection of the YIG magnetization, and W is the measured linewidth of the ferromagnetic resonance. The dependence on the external magnetic field H enters through the NV ESR frequencies $f_- = 2.87 - \tilde{\gamma}H/2\pi$ and the field-dependent magnon dispersion $f(k,\phi_k)$ of the YIG thin film. The measured field-dependence of Γ_- can be well-fitted by Eq. (S28), by which the NV-to-sample distance d is determined to be 250 ± 6 nm and 185 ± 5 nm for NV$_1$ and NV$_2$, respectively. We note that the van der Waals bonding of the diamond nanobeams to the sample surface ensures a same NV-to-sample distance when diamond nanobeams are transferred on the surface of the α-Fe$_2$O$_3$ crystal.

Section S4. Calculation of the Spin Conductivity of α-Fe$_2$O$_3$

To calculate the spin conductivity σ of α-Fe$_2$O$_3$ from the obtained spin diffusion constant D, we invoke the Einstein relation:

$$\sigma = D \frac{\partial \rho}{\partial \mu} \qquad (S29)$$

where ρ is the non-equilibrium magnon spin density. In an approximately $U(1)$-symmetric antiferromagnetic system, the two degenerate magnon modes carrying spin quantum numbers ± 1 can be assigned chemical potential $\pm \mu$ respectively (*21*). Therefore, below the Morin transition, the total spin density can be written as (*51*):

$$\rho = \int \frac{d\vec{k}}{(2\pi)^3} \left[\frac{1}{e^{\beta(\hbar\omega_k - \mu)} - 1} - \frac{1}{e^{\beta(\hbar\omega_k + \mu)} - 1} \right], \qquad (S30)$$

where $\omega_k = \sqrt{v^2 k^2 + \Delta^2}$, $v \sim 3 \times 10^4$ m/s is the spin-wave velocity (*44*), and $\Delta \sim 200$ GHz is the spin-wave gap of α-Fe$_2$O$_3$ at low temperature. Derived from Eq. (S30):

$$\frac{\partial \rho}{\partial \mu} = \frac{(k_B T)^2}{\pi^2 v^3} \left[Li_2 (e^{-\Delta_\alpha / k_B T}) + Li_2 (e^{-\Delta_\beta / k_B T}) \right], \tag{S31}$$

where $\Delta_{\alpha(\beta)} = \Delta \pm \Delta_B$ and $Li_2 (e^{-\Delta / k_B T})$ is the polylogarithmic function of order 2. We have substituted in $\mu = \Delta_B = \gamma H$, which is the frequency gap between the two magnon modes set by the magnetic field. Note that $\Delta \gg \Delta_B$ in our measurement, so we can replace $\Delta_{\alpha(\beta)}$ with Δ in Eq. (S31). Taking the spin diffusion constant measured by our NV relaxometry measurements $D = 8.9 \times 10^{-4}$ m^2/s and $T = 200$ K, the spin conductivity σ is calculated in the unit of electric conductivity by multiplying $\frac{1}{\hbar} \left(\frac{2e}{\hbar} \right)^2$:

$$\sigma = \frac{1}{\hbar} \left(\frac{2e}{\hbar} \right)^2 D \frac{\partial \rho}{\partial \mu} \sim 6.57 \times 10^6 \, S/m. \tag{S32}$$

We remark that the obtained σ is comparable to the value of ferrimagnetic insulator Y$_3$Fe$_5$O$_{12}$ (*21*), suggesting a large spin transport capability of antiferromagnetic insulator α-Fe$_2$O$_3$.

Above the Morin transition temperature, the acoustic spin wave mode introduced by the canted magnetic moment will generate a reduced spin wave gap: $\Delta' \sim \sqrt{2 H_E H_A} \approx 12$ GHz, where H_E is the exchange field and H_A is the effective field associated with the basal plane anisotropy. The resonant frequency of the other optical mode is approximately: $\sqrt{2 H_E H_{A'}} \approx 200$ GHz, where $H_{A'}$ is the anisotropy field along the hard axis. In this case the magnon bands no longer carry good spin quantum numbers, yet as a crude estimation,

$$\sigma \sim \frac{1}{\hbar} \left(\frac{2e}{\hbar} \right)^2 D \frac{(k_B T)^2}{\pi^2 v^3} \left[Li_2 (e^{-\Delta / k_B T}) + Li_2 (e^{-\Delta' / k_B T}) \right] \tag{S33}$$

yields a spin conductivity of 10.14×10^6 S/m at 265 K by substituting the experimentally measured spin diffusion constant and spin wave velocity $v \sim 3 \times 10^4$ m/s (*44*). The estimated spin conductivity does not show a significant variation across the Morin transition in comparison with the value of 9.36×10^6 S/m calculated at 260 K, as expected, since the spin transport is dominated by the exchange energy at a temperature much larger than the magnon gaps.

Section S5. NV Relaxometry to Probe the Magnetic Phase Transition of α-Fe$_2$O$_3$

Next, we briefly discuss how to use NV relaxometry to probe the magnetic phase transition in α-Fe$_2$O$_3$. In our experiments, we aligned NV axis in the (0001)-plane of α-Fe$_2$O$_3$. Using the theoretical model developed in section 2, when T is below the Morin transition temperature ($T_M \sim$ 263 K), the Néel order parameter of α-Fe$_2$O$_3$ is along the x-axis [0001] as illustrated in Fig. S8A with $\vartheta = \pi / 2$, $\varphi = 0$, $\theta = 59$ degree (the relative NV-axis orientation in our measurements). The pre-factor characterizing the coupling strength between an NV center and magnetic fluctuations

in α-Fe$_2$O$_3$ [Eq. (S16)] is given by $f(\theta, \frac{\pi}{2}, 0) = \frac{(\gamma\tilde{\gamma})^2 \pi}{8}(11 - 3\cos 2\theta)$. When $T > T_M$, the Néel order parameter lies in the y-z plane perpendicular to the NV center with $\vartheta = \pi/2 - \theta$, $\varphi = 3\pi/2$, $\theta = 59$ degree, (Fig. S8B), and $f(\theta, \pi/2 - \theta, 3\pi/2) = (\gamma\tilde{\gamma})^2 \pi (61 - 32\cos 2\theta + 3\cos 4\theta)/32$. To illustrate the variation of the NV relaxation rate induced by the rotation of the Néel order parameter, Fig. S8C plots the temperature dependent NV relaxation rate Γ_- measured between 200 K and 300 K. Because Γ_+ is significantly smaller than Γ_-, we use Γ_- to monitor the Morin transition of α-Fe$_2$O$_3$. The external magnetic field H is set to be 683 Oe, corresponding to an NV ESR frequency f_- of 0.96 GHz. In general, Γ_- increases with the temperature indicating that the magnetic noise scales with the temperature as shown in Eq. (S15). Notably, at the temperature near 263 K, we observed a sudden jump of Γ_-, which is attributable to the rotation of the Néel order parameter during the Morin transition. Overall, the experimental results agree well with the theoretical predication based on Eq. (S26), as illustrated by the blue dash line. Note that the Morin transition of α-Fe$_2$O$_3$ is treated as a step change of the magnetic orientation at 263 K in our model. In reality, the observed transition could be more gradual (as shown in the experimental results) due to inhomogeneity and multidomain structures. Note that magnetic domains with dimensions comparable or smaller than the NV-to-sample distance could emerge when the measurement temperature is close to the Morin transition point. In this situation, we actually measure an average effect of the multi-domains experienced by the NV center. This could explain the gradual variation of the measured NV relaxation rate across the Morin transition point. The discrepancy of $\Delta\Gamma_-/\Gamma_-$ around 263 K between the experimental result (~20%) and the theoretical value (~50%) can be induced by the variation of the static longitudinal magnetic susceptibility during the Morin transition and imperfection of the magnetic orientation. We note that our theoretical model assumes all other factors remain the same in the studied temperature range, which is unlikely in the real experiment. Therefore, we are not looking for a quantitative agreement of the theoretical model to the experimental results, but a qualitative consistency.

**Section S6. Direct Comparison Between Transverse and Longitudinal Spin Fluctuations**

The minimal magnon energies in both canted antiferromagnetic and easy-axis antiferromagnetic phases of α-Fe$_2$O$_3$ are larger than the NV ESR frequencies in our accessible magnetic field range. Thus, it is challenging to directly compare the transverse and longitudinal spin fluctuations of α-Fe$_2$O$_3$. Next, we resort to conventional ferrimagnetic insulator Y$_3$Fe$_5$O$_{12}$, whose magnon gap can be effectively tuned below and above the NV ESR frequency in the low magnetic field range (0 Oe $< H <$ 1000 Oe) for this study. Figure S9A plots the ferromagnetic resonance (FMR) frequency f_{FMR} of a 20-nm-thick Y$_3$Fe$_5$O$_{12}$ film and the NV ESR frequencies $f_\pm$ as a function of magnetic field H. The external magnetic field is applied along the NV-axis. When $H < 320$ Oe, the NV ESR frequency f_- is above f_{FMR}, thus, transverse spin fluctuations mediated resonant NV-magnon coupling dominates. When $H > 320$ Oe, f_- lies below the minimum magnon energy set by f_{FMR}. In this situation, NV-magnon coupling is established by the longitudinal spin fluctuations. Figures S9B and S9C show the magnon dispersion of the 20-nm-thick Y$_3$Fe$_5$O$_{12}$ film in these two distinct experimental conditions. Figure S9D shows the measured NV relaxation rate as a function of the external magnetic field. Not surprisingly, the magnitude of the one-magnon scattering noise induced by transverse spin fluctuations is significantly larger than

that of the two-magnon scattering noise induced by longitudinal spin fluctuations. By fitting the field dependent one-magnon noise in the low field regime ($H < 320$ Oe) with Eq. (S28), we are able to estimate the NV-to-sample distance as discussed in Section 3.

Focusing on the high magnetic field regime ($H > 320$ Oe) where the two-magnon scattering noise dominates, we can extract the intrinsic spin diffusion constant of the $Y_3Fe_5O_{12}$ film. Figure S9E plots the longitudinal spin fluctuation induced NV relaxation rate as a function of external magnetic field ($H > 320$ Oe). By fitting our experimental results to the following equation in the $l_s \gg d$ regime ([38]):

$$\Gamma_-(f_-) \sim \frac{\hbar f(\theta)}{Dd^2} \frac{k_\mathrm{B} T \chi_0}{1 + \left(\frac{2\pi f_- d^2}{D}\right)^2}$$ (S34)

where $f(\theta)$ is a geometric factor ([38]), k_B is the Boltzmann constant, $\hbar$ is the reduced Planck constant, the spin diffusion constant D of the 20-nm-thick $Y_3Fe_5O_{12}$ thin film is measured to be $(1.5 \pm 0.4) \times 10^{-5}$ m^2/s, in qualitative agreement with the results obtained by previous electrical transport study ([21]). Here, we note that the thickness of the $Y_3Fe_5O_{12}$ thin film is considerably smaller than the NV-to-sample distance, thus, we do not consider the variation of the spin density along the thickness direction of the $Y_3Fe_5O_{12}$ sample. The detailed derivation processes of Eq. S34 can be found in Ref. 38 and its Supplemental Materials.
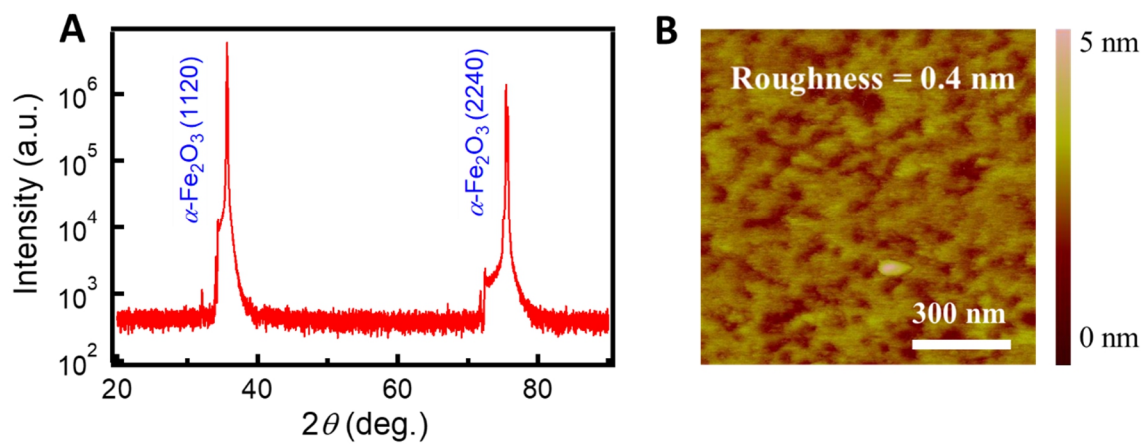
Figure S1. **Structural and surface characterizations of α-Fe₂O₃ sample.** (**A**) $\theta - 2\theta$ x-ray diffraction scan of an α-Fe₂O₃ (1120) crystal. (**B**) Atomic force microscopy image of a polished surface of the α-Fe₂O₃ (1120) crystal over an area of 1 μm × 1 μm.
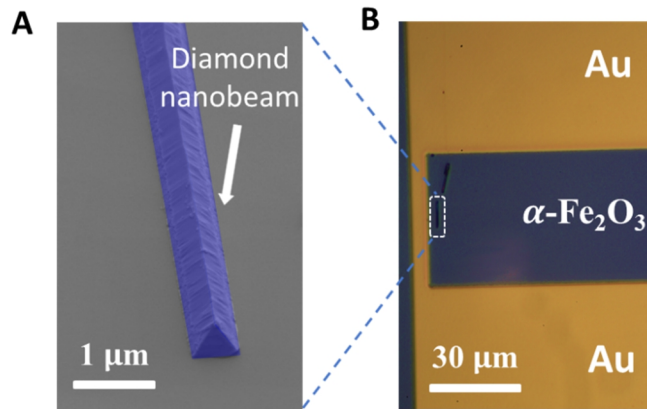
Figure S2. **Scanning electron microscopy and optical images of a prepared NV-α-Fe$_2$O$_3$ device**. (**A**) A scanning electron microscope image of a patterned diamond nanobeam (false-colored blue) positioned on top of a sample surface. (**B**) An optical image of a prepared NV-α-Fe$_2$O$_3$ sample. The white dashed line is used to mark the position of a transferred diamond nanobeam, which is in vicinity of the patterned on-chip Au stripline.
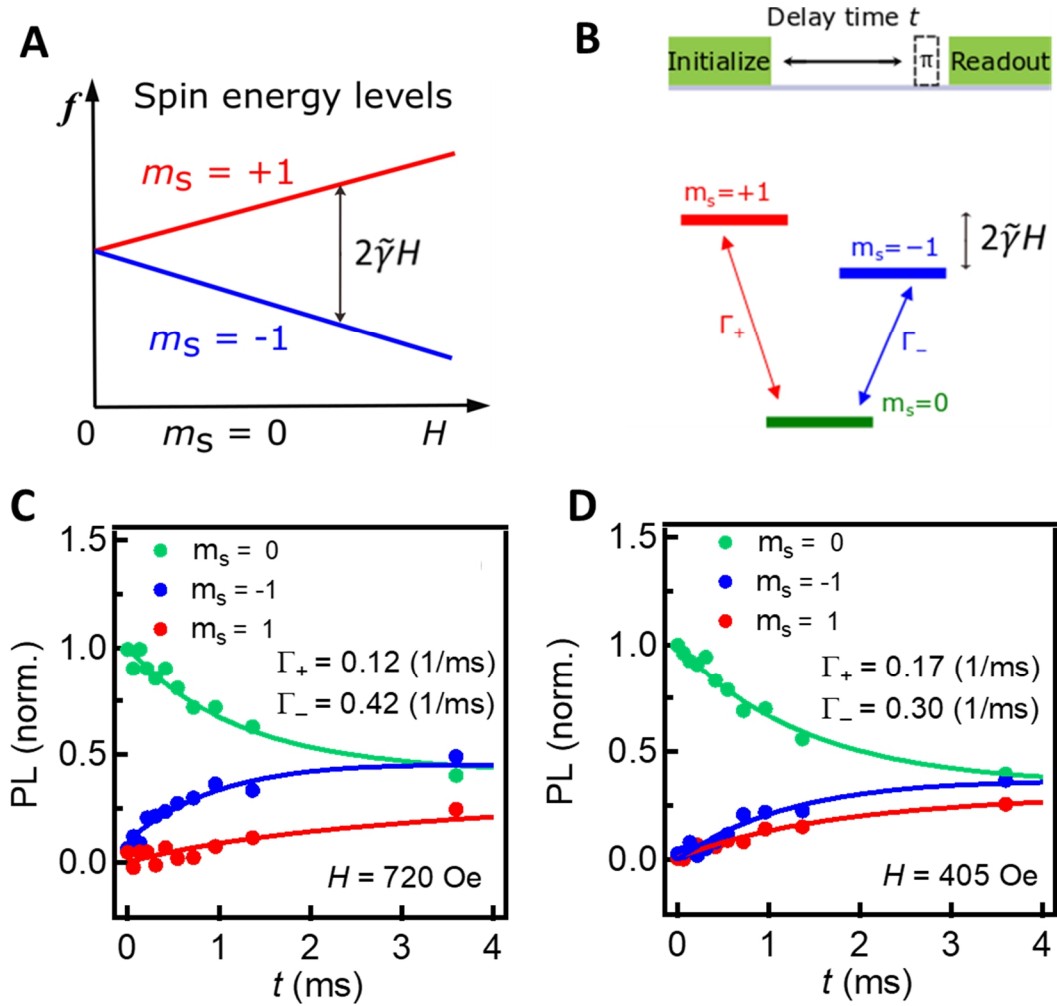
Figure S3. **Illustration of NV relaxation and experimental results.** (**A**) An energy diagram of an NV spin as a function of external field H applied along the NV-axis. (**B**) Top: Pulse sequence of the NV relaxometry measurements. Bottom: Schematic to illustrate the spin relaxation in a three-level quantum system. (**C**, **D**) Time dependence of the measured PL signal of NV$_1$ at H = 720 Oe and 405 Oe.
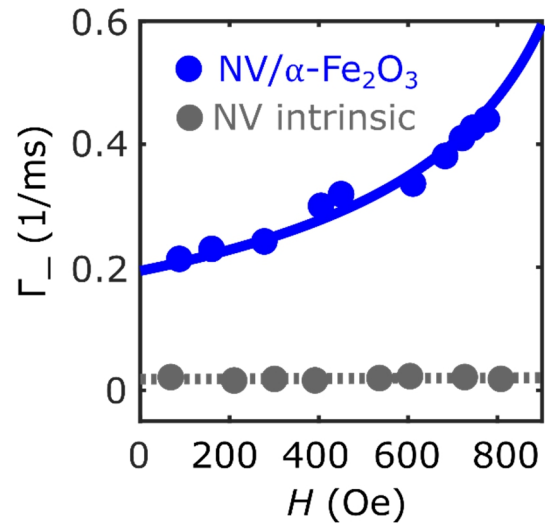
Figure S4. **Comparison of intrinsic NV relaxation rate with that measured on α-Fe$_2$O$_3$.** Magnetic field dependence of the NV relaxation rate Γ_- measured on α-Fe$_2$O$_3$ (blue curve) and on a nonmagnetic substrate SiO$_2$ (grey curve).
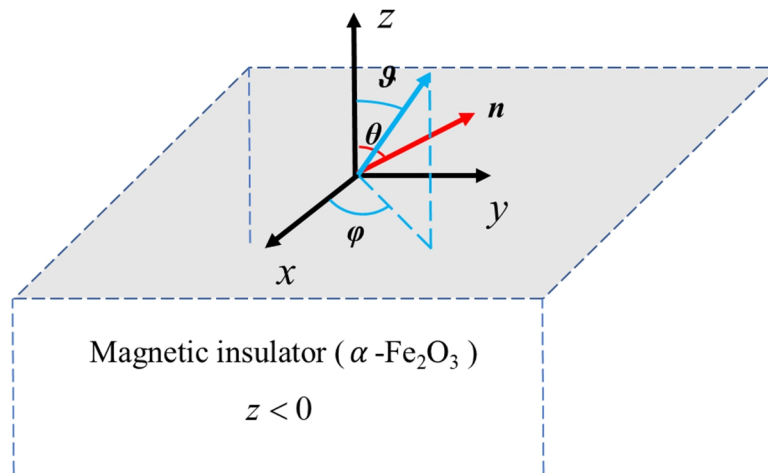
Figure S5. **Schematic of the relative NV orientation and Néel order parameter for theoretical analysis**. The coordinate system used to analyze the NV relaxation induced by the longitudinal spin fluctuations of a proximal magnetic insulator (α-Fe$_2$O$_3$). The blue arrow represents the orientation of the Néel order parameter and the red arrow represents the orientation of the NV center.
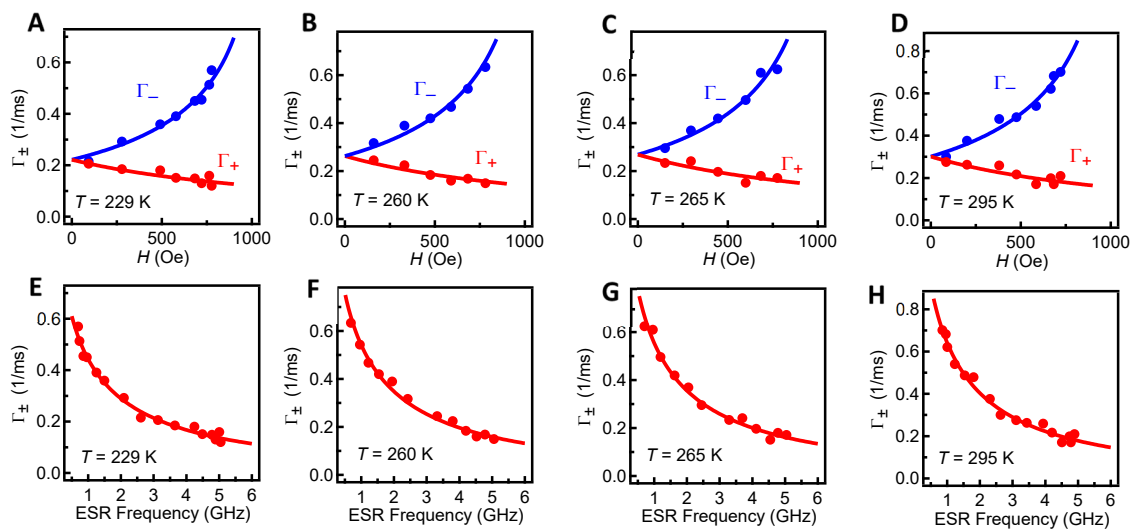
Figure S6. **NV relaxometry results measured at different temperatures**. (**A-H**): Magnetic field and ESR frequency dependence of the NV relaxation rates $\Gamma_{\pm}$ measured at $T = 229$, 260, 265, and 295 K. At all temperatures, the variations of $\Gamma_{\pm}$ are well fitted using our theory as shown by the red and blue curves, by which the intrinsic spin diffusion constant of α-Fe_2O_3 can be extracted.
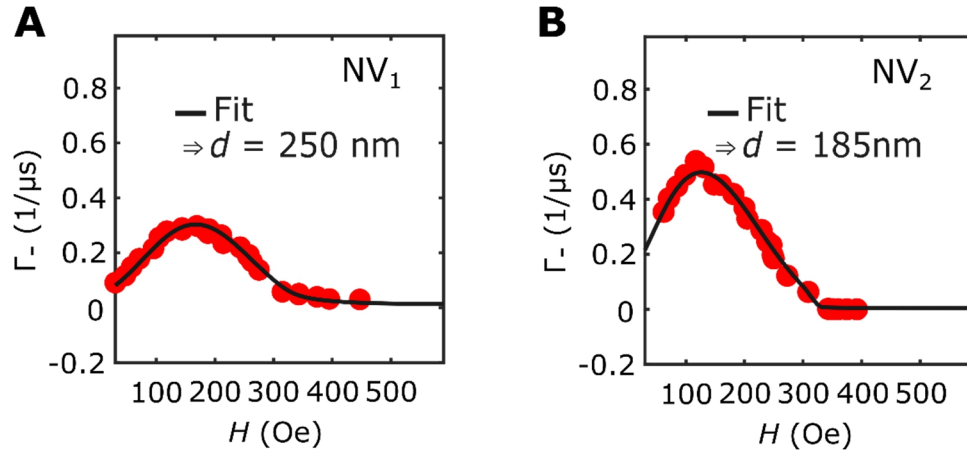
Figure S7. **Calibration of NV-to-sample-surface distance**. Diamond nanobeams are transferred on top of a 100-nm-thick YIG thin film to characterize the NV-to-sample distance d. Relaxation rates Γ_- of (**A**) NV_1 and (**B**) NV_2 measured as a function of external magnetic field H. By fitting the curves to Eq. (S28), d is characterized to be 250 ± 6 nm and 185 ± 5 nm for NV_1 and NV_2, respectively.

Figure S8. **Magnetic phase transition probed by NV Relaxometry**. (**A**, **B**) Schematic to illustrate the Néel order orientation of α-Fe$_2$O$_3$ relative to the NV-axis below and above the Morin temperature (T_M). The blue arrow represents the orientation of the Néel order parameter an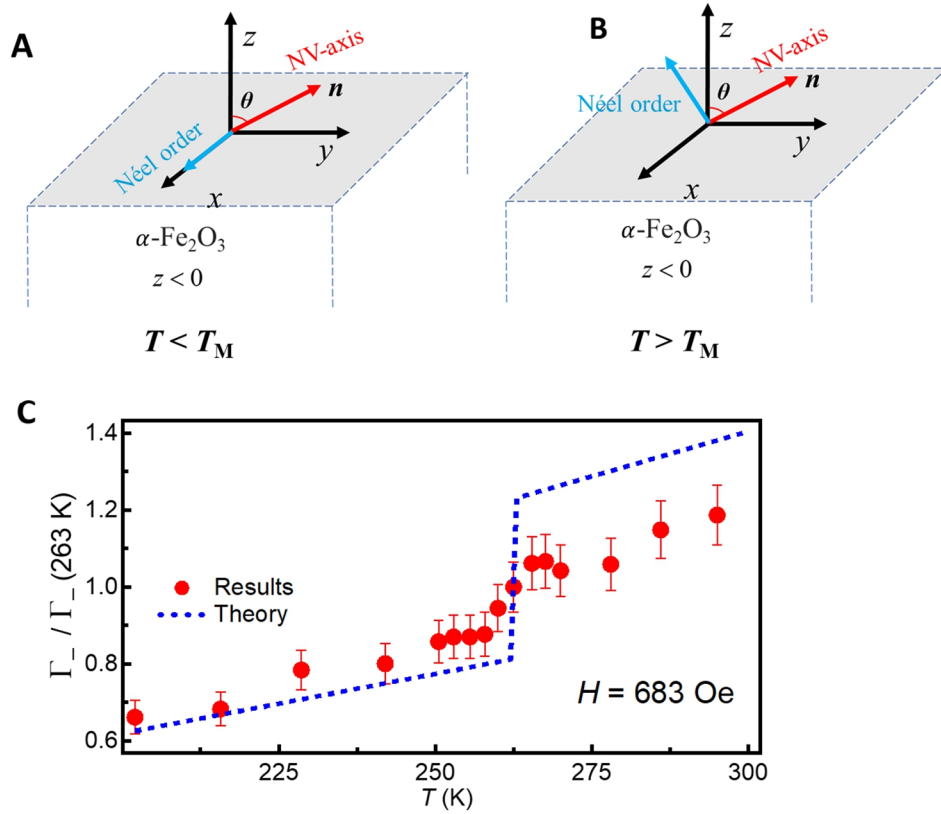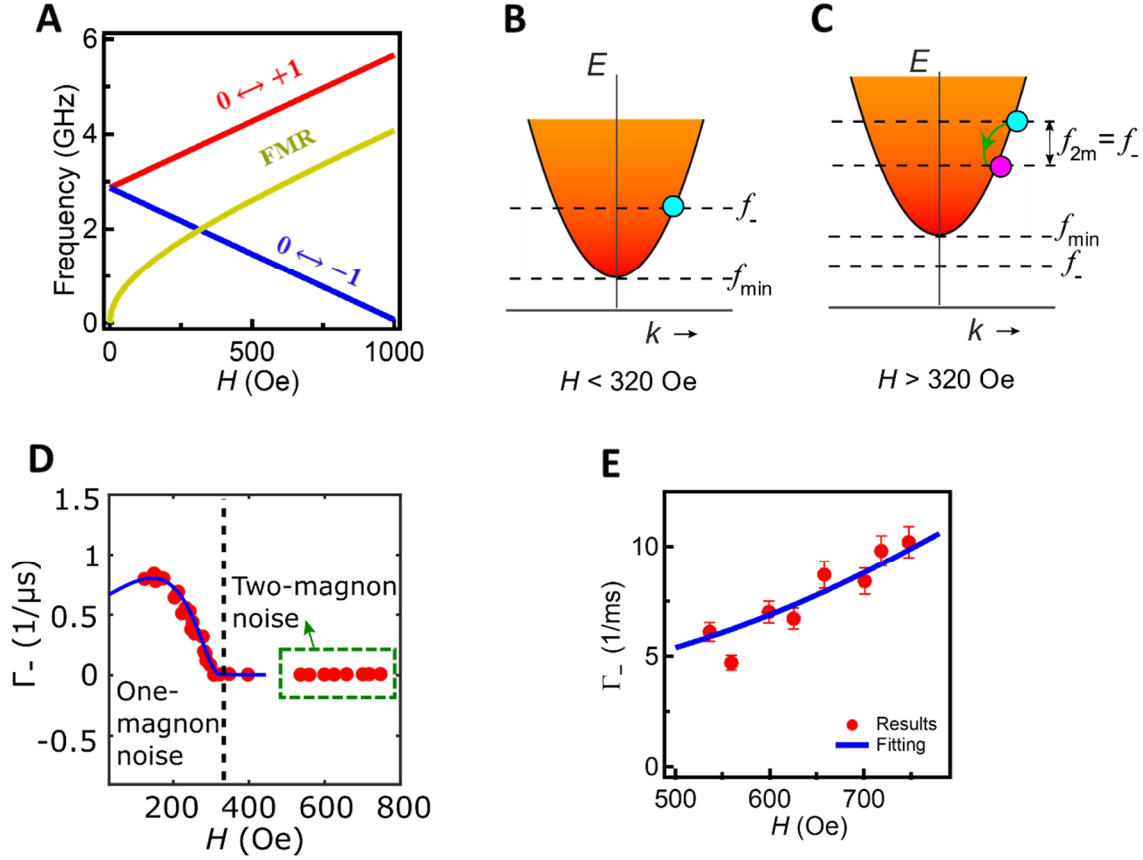d the red arrow represents the orientation of the NV center. (**C**) Variation of the NV relaxation rate $\Gamma_-/\Gamma_-(263$ K) measured as a function of temperature between 200 K and 300 K when $H = 683$ Oe. Γ_- corresponds to the NV relaxation rate of the $m_s = 0 \leftrightarrow -1$ transition. The blue dash line is the theoretical predication based on Eq. (S26).

Figure S9. **Direct comparison between longitudinal and transverse spin fluctuations in $Y_3Fe_5O_{12}$.** (**A**) FMR frequency f_{FMR} of a 20-nm-thick $Y_3Fe_5O_{12}$ thin film and the NV ESR frequencies $f_\pm$ as a function of external magnetic field H. Schematic of magnon dispersion of a 20-nm-thick $Y_3Fe_5O_{12}$ film when (**B**) $H < 320$ Oe and (**C**) $H > 320$ Oe. The NV ESR frequency f_- is above and below the minimal magnon energy f_{min} set by f_{FMR}, respectively. (**D**) Measured NV spin relaxation rate Γ_- as a function of external magnetic field H. The black dash line marks the transition magnetic field between the resonant and non-resonant NV-magnon coupling. (**E**) Obtained spin relaxation rates Γ_- as a function of magnetic field when $H > 320$ Oe, which is in agreement with a theoretical model (blue curves). The obtained spin diffusion constant of a 20-nm-thick $Y_3Fe_5O_{12}$ film is $(1.5 \pm 0.4) \times 10^{-5}$ m^2/s.

REFERENCES AND NOTES

1. V. Baltz, A. Manchon, M. Tsoi, T. Moriyama, T. Ono, Y. Tserkovnyak, Antiferromagnetic spintronics. *Rev. Mod. Phys.* **90**, 015005 (2018).

2. T. Jungwirth, J. Sinova, A. Manchon, X. Marti, J. Wunderlich, C. Felser, The multiple directions of antiferromagnetic spintronics. *Nat. Phys.* **14**, 200–203 (2018).

3. S. M. Rezende, A. Azevedo, R. L. Rodríguez-Suárez, Introduction to antiferromagnetic magnons. *J. Appl. Phys.* **126**, 151101 (2019).

4. J. Li, C. B. Wilson, R. Cheng, M. Lohmann, M. Kavand, W. Yuan, M. Aldosary, N. Agladze, P. Wei, M. S. Sherwin, J. Shi, Spin current from sub-terahertz-generated antiferromagnetic magnons. *Nature* **578**, 70–74 (2020).

5. P. Vaidya, S. A. Morley, J. van Tol, Y. Liu, R. Cheng, A. Brataas, D. Lederman, E. del Barco, Subterahertz spin pumping from an insulating antiferromagnet. *Science* **368**, 160–165 (2020).

6. S. M. Wu, W. Zhang, A. Kc, P. Borisov, J. E. Pearson, J. S. Jiang, D. Lederman, A. Hoffmann, A. Bhattacharya, Antiferromagnetic spin Seebeck effect. *Phys. Rev. Lett.* **116**, 097204 (2016).

7. W. Zhang, M. B. Jungfleisch, W. Jiang, J. E. Pearson, A. Hoffmann, F. Freimuth, Y. Mokrousov, Spin Hall effects in metallic antiferromagnets. *Phys. Rev. Lett.* **113**, 196602 (2014).

8. T. Kosub, M. Kopte, R. Hühne, P. Appel, B. Shields, P. Maletinsky, R. Hübner, M. O. Liedke, J. Fassbender, O. G. Schmidt, D. Makarov, Purely antiferromagnetic magnetoelectric random access memory. *Nat. Commun.* **8**, 13985 (2017).

9. P. Wadley, B. Howells, J. Železný, C. Andrews, V. Hills, R. P. Campion, V. Novák, K. Olejník, F. Maccherozzi, S. S. Dhesi, S. Y. Martin, T. Wagner, J. Wunderlich, F. Freimuth, Y. Mokrousov, J. Kuneš, J. S. Chauhan, M. J. Grzybowski, A. W. Rushforth, K. Edmond, B.

L. Gallagher, T. Jungwirth, Electrical switching of an antiferromagnet. *Science* **351**, 587–590 (2016).

10. Y. Cheng, S. Yu, M. Zhu, J. Hwang, F. F. Yang, Electrical switching of tristate antiferromagnetic Néel order in α-Fe$_2$O$_3$ epitaxial films. *Phys. Rev. Lett.* **124**, 027202 (2020).

11. X. Z. Chen, R. Zarzuela, J. Zhang, C. Song, X. F. Zhou, G. Y. Shi, F. Li, H. A. Zhou, W. J. Jiang, F. Pan, Y. Tserkovnyak, Antidamping-torque-induced switching in biaxial antiferromagnetic insulators. *Phys. Rev. Lett.* **120**, 207204 (2018).

12. M. S. Wörnle, P. Welter, Z. Kašpar, K. Olejník, V. Novák, R. P. Campion, P. Wadley, T. Jungwirth, C. L. Degen, P. Gambardella, Current-induced fragmentation of antiferromagnetic domains (2019); http://arxiv.org/abs/1912.05287.

13. I. Gray, T. Moriyama, N. Sivadas, G. M. Stiehl, J. T. Heron, R. Need, B. J. Kirby, D. H. Low, K. C. Nowack, D. G. Schlom, D. C. Ralph, T. Ono, G. D. Fuchs, Spin Seebeck imaging of spin-torque switching in antiferromagnetic Pt/NiO heterostructures. *Phys. Rev. X* **9**, 041016 (2019).

14. C. C. Chiang, S. Y. Huang, D. Qu, D. P. H. Wu, C. L. Chien, Absence of evidence of electrical switching of the antiferromagnetic Néel vector. *Phys. Rev. Lett.* **123**, 227203 (2019).

15. R. Lebrun, A. Ross, S. A. Bender, A. Qaiumzadeh, L. Baldrati, J. Cramer, A. Brataas, R. A. Duine, M. Kläui, Tunable long-distance spin transport in a crystalline antiferromagnetic iron oxide. *Nature* **561**, 222–225 (2018).

16. W. Yuan, Q. Zhu, T. Su, Y. Yao, W. Xing, Y. Chen, Y. Ma, X. Lin, J. Shi, R. Shindou, X. C. Xie, W. Han, Experimental signatures of spin superfluid ground state in canted antiferromagnet Cr$_2$O$_3$ via nonlocal spin transport. *Sci. Adv.* **4**, eaat1098 (2018).

17. R. Lebrun, A. Ross, O. Gomonay, V. Baltz, U. Ebels, A. L. Barra, A. Qaiumzadeh, A. Brataas, J. Sinova, M. Kläui, Long-distance spin-transport across the Morin phase transition

up to room temperature in the ultra-low damping single crystals of the antiferromagnet α-Fe_2O_3. *Nat. Commun.* **11**, 6332 (2020).

18. T. Wimmer, A. Kamra, J. Gückelhorn, M. Opel, S. Geprägs, R. Gross, H. Huebl, M. Althammer, Observation of antiferromagnetic magnon pseudospin dynamics and the Hanle effect. *Phys. Rev. Lett.* **125**, 247204 (2020).

19. J. Han, P. Zhang, Z. Bi, Y. Fan, T. S. Safi, J. Xiang, J. Finley, L. Fu, R. Cheng, L. Liu, Birefringence-like spin transport via linearly polarized antiferromagnetic magnons. *Nat. Nanotechnol.* **15**, 563–568 (2020).

20. L. J. Cornelissen, J. Liu, R. A. Duine, J. Ben Youssef, B. J. van Wees, Long-distance transport of magnon spin information in a magnetic insulator at room temperature. *Nat. Phys.* **11**, 1022–1026 (2015).

21. L. J. Cornelissen, K. J. H. Peters, G. E. W. Bauer, R. A. Duine, B. J. van Wees, Magnon spin transport driven by the magnon chemical potential in a magnetic insulator. *Phys. Rev. B* **94**, 014412 (2016).

22. B. L. Giles, Z. Yang, J. S. Jamison, R. C. Myers, Long-range pure magnon spin diffusion observed in a nonlocal spin-Seebeck geometry. *Phys. Rev. B* **92**, 224415 (2015).

23. K. S. Burch, D. Mandrus, J.-G. Park, Magnetism in two-dimensional van der Waals materials. *Nature* **563**, 47–52 (2018).

24. W. Wang, M. W. Daniels, Z. Liao, Y. Zhao, J. Wang, G. Koster, G. Rijnders, C.-Z. Chang, D. Xiao, W. Wu, Spin chirality fluctuation in two-dimensional ferromagnets with perpendicular magnetic anisotropy. *Nat. Mater.* **18**, 1054–1059 (2019).

25. L. Savary, L. Balents, Quantum spin liquids: A review. *Rep. Prog. Phys.* **80**, 016502 (2017).

26. S. Nakatsuji, N. Kiyohara, T. Higo, Large anomalous Hall effect in a non-collinear antiferromagnet at room temperature. *Nature* **527**, 212–215 (2015).

27. S. Zhang, Y. Tserkovnyak, Flavors of noise in magnetic Weyl semimetals (2021); https://arxiv.org/abs/2108.07305.

28. L. Rondin, J.-P. Tetienne, T. Hingant, J.-F. Roch, P. Maletinsky, V. Jacques, Magnetometry with nitrogen-vacancy defects in diamond. *Reports Prog. Phys.* **77**, 056503 (2014).

29. G. Q. Liu, X. Feng, N. Wang, Q. Li, R. B. Liu, Coherent quantum control of nitrogen-vacancy center spins near 1000 kelvin. *Nat. Commun.* **10**, 1344 (2019).

30. A. Laraoui, H. Aycock-Rizzo, Y. Gao, X. Lu, E. Riedo, C. A. Meriles, Imaging thermal conductivity with nanoscale resolution using a scanning spin probe. *Nat. Commun.* **6**, 8954 (2015).

31. M. Pelliccione, A. Jenkins, P. Ovartchaiyapong, C. Reetz, E. Emmanouilidou, N. Ni, A. C. Bleszynski Jayich, Scanned probe imaging of nanoscale magnetism at cryogenic temperatures with a single-spin quantum sensor. *Nat. Nanotechnol.* **11**, 700–705 (2016).

32. L. Thiel, Z. Wang, M. A. Tschudin, D. Rohner, I. Gutiérrez-Lezama, N. Ubrig, M. Gibertini, E. Giannini, A. F. Morpurgo, P. Maletinsky, Probing magnetism in 2D materials at the nanoscale with single-spin microscopy. *Science* **364**, 973–976 (2019).

33. M. J. Burek, N. P. de Leon, B. J. Shields, B. J. M. Hausmann, Y. Chu, Q. Quan, A. S. Zibrov, H. Park, M. D. Lukin, M. Lončar, Free-standing mechanical and photonic nanostructures in single-crystal diamond. *Nano Lett.* **12**, 6084–6089 (2012).

34. C. H. R. Du, T. Van der Sar, T. X. Zhou, P. Upadhyaya, F. Casola, H. Zhang, M. C. Onbasli, C. A. Ross, R. L. Walsworth, Y. Tserkovnyak, A. Yacoby, Control and local measurement of the spin chemical potential in a magnetic insulator. *Science* **357**, 195–198 (2017).

35. E. Lee-Wong, R. L. Xue, F. Y. Ye, A. Kreisel, T. van der Sar, A. Yacoby, C. H. R. Du, Nanoscale detection of magnon excitations with variable wavevectors through a quantum spin sensor. *Nano Lett.* **20**, 3284–3290 (2020).

36. G. D. Fuchs, V. V. Dobrovitski, D. M. Toyli, F. J. Heremans, D. D. Awschalom, Gigahertz dynamics of a strongly driven single quantum spin. *Science* **326**, 1520–1522 (2009).

37. T. Holstein, H. Primakoff, Field dependence of the intrinsic domain magnetization of a ferromagnet. *Phys. Rev.* **58**, 1098–1113 (1940).

38. B. Flebus, Y. Tserkovnyak, Quantum-impurity relaxometry of magnetization dynamics. *Phys. Rev. Lett.* **121**, 187204 (2018).

39. B. A. McCullian, A. M. Thabt, B. A. Gray, A. L. Melendez, M. S. Wolf, V. L. Safonov, D. V. Pelekhov, V. P. Bhallamudi, M. R. Page, P. C. Hammel, Broadband multi-magnon relaxometry using a quantum spin sensor for high frequency ferromagnetic dynamics sensing. *Nat. Commun.* **11**, 5229 (2020).

40. S. S. L. Zhang, S. Zhang, Magnon mediated electric current drag across a ferromagnetic insulator layer. *Phys. Rev. Lett.* **109**, 096603 (2012).

41. M. R. Page, F. Guo, C. M. Purser, J. G. Schulze, T. M. Nakatani, C. S. Wolfe, J. R. Childress, P. C. Hammel, G. D. Fuchs, V. P. Bhallamudi, Optically detected ferromagnetic resonance in diverse ferromagnets via nitrogen vacancy centers in diamond. *J. Appl. Phys.* **126**, 124902 (2019).

42. J. P. Tetienne, T. Hingant, L. Rondin, A. Cavaillès, L. Mayer, G. Dantelle, T. Gacoin, J. Wrachtrup, J. F. Roch, V. Jacques, Spin relaxometry of single nitrogen-vacancy defects in diamond nanocrystals for magnetic noise sensing. *Phys. Rev. B* **87**, 235436 (2013).

43. T. van der Sar, F. Casola, R. Walsworth, A. Yacoby, Nanometre-scale probing of spin waves using single-electron spins. *Nat. Commun.* **6**, 7886 (2015).

44. E. J. Samuelsen, G. Shirane, Inelastic neutron scattering investigation of spin waves and magnetic interactions in α-Fe$_2$O$_3$. *Phys. Status Solidi B* **42**, 241–256 (1970).

45. K. Shen, Magnon spin relaxation and spin Hall effect due to the dipolar interaction in antiferromagnetic insulators. *Phys. Rev. Lett.* **124**, 077201 (2020).

46. P. R. Elliston, G. J. Troup, Some antiferromagnetic resonance measurements in α-Fe$_2$O$_3$. *J. Phys. C* **1**, 169–178 (1968).

47. S. Chatterjee, J. F. Rodriguez-Nieva, E. Demler, Diagnosing phases of magnetic insulators via noise magnetometry with spin qubits. *Phys. Rev. B* **99**, 104425 (2019).

48. D. B. Bucher, D. P. L. Aude Craik, M. P. Backlund, M. J. Turner, O. Ben Dor, D. R. Glenn, R. L. Walsworth, Quantum diamond spectrometer for nanoscale NMR and ESR spectroscopy. *Nat. Protoc.* **14**, 2707–2747 (2019).

49. K. Y. Guslienko, A. N. Slavin, Magnetostatic Green's functions for the description of spin waves in finite rectangular magnetic dots and stripes. *J. Magn. Magn. Mater.* **323**, 2418–2424 (2011).

50. A. Rustagi, I. Bertelli, T. van der Sar, P. Upadhyaya, Sensing chiral magnetic noise via quantum impurity relaxometry. *Phys. Rev. B* **102**, 220403(R) (2020).

51. B. Flebus, Chemical potential of an antiferromagnetic magnon gas. *Phys. Rev. B* **100**, 064410 (2019).